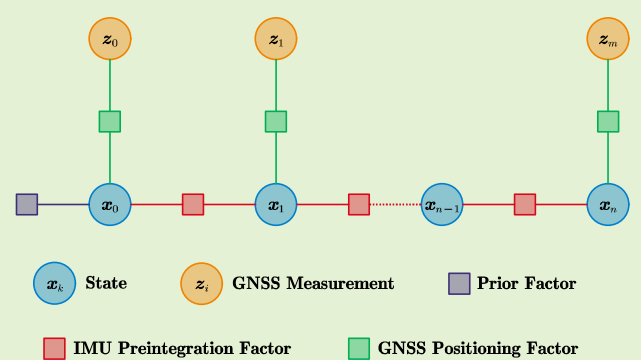


Impact of the Earth Rotation Compensation on MEMS-IMU Preintegration of Factor Graph Optimization

Hailiang Tang, Tisheng Zhang, Xiaoji Niu, Jing Fan, and Jingnan Liu

Abstract—In filtering-based global navigation satellite system (GNSS) / inertial navigation system (INS) integrated navigation systems, the precise INS mechanization has fully considered the impact of the Earth rotation, Coriolis acceleration, etc. However, most inertial measurement unit (IMU) preintegration models in factor graph optimization (FGO)-based integrated navigation systems are rough and ignore these factors. We propose an FGO-based GNSS/INS integrated navigation system to analyze and evaluate the impact of the Earth rotation on MEMS-IMU preintegration. The proposed FGO-based integration is based on a refined IMU preintegration, in which the Earth rotation is compensated. The proposed GNSS/INS integration is a sliding-window optimizer in which the GNSS positioning and the IMU preintegration are tightly fused within the FGO framework. The simulated GNSS outage in field tests, an effective method, is adopted to evaluate the IMU preintegration quantitatively. The results demonstrate that the refined IMU preintegration can achieve the same accuracy as the precise INS mechanization. In contrast, the rough IMU preintegration and INS mechanization without compensating for the Earth rotation yields notable accuracy degradation. When the GNSS-outage time is 60 seconds, the degradation can be 200% for the industrial-grade MEMS module and more than 10% for the consumer-grade MEMS chip. Besides, the degradation can be more significant if the GNSS-outage time is longer. The proposed FGO-based GNSS/INS integration (https://github.com/i2Nav-WHU/OB_GINS) and the employed datasets (<https://github.com/i2Nav-WHU/awesome-gins-datasets>) are open-sourced on GitHub.



Index Terms—MEMS-IMU preintegration, factor graph optimization, GNSS/INS integration.

I. INTRODUCTION

Inertial measurement unit (IMU) has been employed in navigation systems since the last century [1], [2]. With the rapid development of micro-electro-mechanical systems (MEMS), MEMS IMU has been widely used in navigation applications because of their low cost, low power consumption, and small size. Some industrial-grade MEMS modules have even achieved close precision compared to the tactical-grade IMU [3]. However, MEMS IMU suffers from significant errors, such as biases and scale factors, resulting in worse accuracy for long-term navigation. Hence, MEMS IMU is usually aided by a global navigation satellite system (GNSS) receiver to construct a GNSS/INS integrated navigation system, which can provide accurate long-term navigation. Traditionally, the GNSS/INS integration has been based on a Kalman filter framework, incorporating the extended Kalman filter (EKF), the unscented

Kalman filter [3], and some novel algorithms, such as self-learning square-root cubature Kalman filter [4] and gybird interacting multiple model [5]. In particular, EKF-based GNSS/INS integration has become a mature technology that constitutes a benchmark for INS accuracy because the Earth rotation, the Coriolis acceleration, and various precise corrections are fully considered in the precise INS mechanization [1]–[3]. In our previous work [6], to reduce the computation load, a simplified INS algorithm, in which only the Earth rotation was compensated, achieved an accuracy degradation of 0.3% for MEMS IMU, compared to the precise INS mechanization using the simulated GNSS outage [7]. The work in [6] indicates that the Earth rotation compensation is essential in maintaining the MEMS-INS accuracy. In contrast, the minor terms in the INS algorithm, including the Coriolis acceleration, the rotation correction, the sculling correction, and the coning correction, can be ignored. Here, the simulated GNSS outage [7] is a standard to evaluate the INS accuracy in the integrated navigation system. The simulated GNSS outage is usually conducted in open-sky areas, where the GNSS positioning tends to be accurate without outliers.

Factor graph optimization (FGO) in robotics [8], [9] or Dynamic Network (DN) in geodesy [10], [11] has been proven to be more accurate and effective than the filtering-based

This research is funded by the National Key Research and Development Program of China (No. 2020YFB0505803), and the National Natural Science Foundation of China (No. 41974024). (Corresponding authors: Xiaoji Niu; Tisheng Zhang.)

Hailiang Tang, Tisheng Zhang, Xiaoji Niu, Jing Fan, and Jingnan Liu, are with the GNSS Research Center, Wuhan University, Wuhan 430079, China (e-mail: thl, zts, xjniu, jingfan, jnliu@whu.edu.cn).

XXXX-XXXX © XXXX IEEE. Personal use is permitted, but republication/redistribution requires IEEE permission. See http://www.ieee.org/publications_standards/publications/rights/index.html for more information.

approaches for solving maximum a posteriori (MAP) estimation, especially in complex and challenging environments. FGO and DN can achieve optimal state estimation by solving non-linear optimization problems [8], [12]. DN is a particular case of FGO because it processes all the measurements simultaneously without marginalization [12]. In the following parts, the non-linear optimization problems in multi-sensor navigation will be expressed as FGO for clarity. Compared to the filtering-based methods, such improvements benefit from the multiple iterations and the time correction of the FGO, as mentioned in [13], [14]. The repeated linearization by iterations can significantly reduce the linearization error for the non-linear observation model. In addition, all the observations in the FGO window can be utilized simultaneously, which can help resist the outliers. However, it has historically been challenging to incorporate IMU into the FGO because of the nature of acceleration measurements and biases [15]. In [13], [16], the FGO was used to achieve a GNSS/INS integration for positioning in urban areas where the GNSS outliers frequently occurred. The results indicated that the FGO-based integration outperformed the EKF-based method. However, a rough INS factor [13], [16], in which the acceleration measurements were employed to constrain velocity, and the gyroscope measurements were employed to constrain orientation, was used in their systems. The INS integration is roughly processed in such INS factor, and the IMU biases have not been considered, not to mention the Earth rotation compensation. These rough processes are a waste of IMU accuracy, even for MEMS IMU.

To overcome these problems, the IMU preintegration has been proposed to utilize the IMU precision fully and further improve the system accuracy. The IMU preintegration was first proposed by Lupton and Sukkarieh [17]. They integrated the IMU measurements in a local reference frame and linearized those measurements about the current bias estimations to construct a relative-constraint factor in FGO. Subsequently, Forster et al. [18] built upon [17] to develop a preintegration model that addressed the manifold structure of the $SO(3)$ rotation group and seamlessly integrated the preintegration model into a visual-inertial pipeline. Similarly, the work in [18] was modified by introducing a non-constant gravity model, the Earth rotation, and the Coriolis force to fuse IMU and GNSS in a Dynamic Network [12]. In related studies [19], [20], IMU on-manifold preintegration was extended to $SE(2)$ Lie group [21] to allow expression of the extended pose (position, velocity, and orientation). Quaternion-based preintegration models have also attracted intense attention [22]–[26]. Quaternion is another representation of the orientation, which can achieve the same function as the manifold. In addition, to overcome the discretization effect, IMU motion integration models in continuous time have also been proposed [15], [27]. Eckenhoff et al. [15] proposed a new analytical preintegration model for the IMU kinematics in continuous time; this approach yielded improved accuracy for the visual-inertial navigation system (VINS). In addition, a switched linear system was used to model the IMU motion in continuous time [27], outperforming the state-of-the-art IMU preintegration models. The in-vehicle sensors, including the wheel speed and steering angle sensor, have also been incorporated into the IMU preintegration to improve vehicle navigation accuracy [25],

[26]. In terms of the INS accuracy, most existing IMU preintegration models are relatively rough, and some precise compensations or corrections, such as the Earth rotation and Coriolis acceleration, have not been well considered. Moreover, the essential factor, the Earth rotation, has not been compensated in these IMU preintegration, which may significantly degrade the INS accuracy even for MEMS IMU, as mentioned above.

The Earth rotation compensation has been considered in recent IMU preintegration models [12], [19], [20], [24] to improve the preintegration accuracy for high-precision IMU, such as tactical-grade and navigation-grade IMU [3]. However, its impact on MEMS IMU is still ambiguous. A reduced IMU preintegration, without velocities estimation, was proposed for GNSS/INS integration in DN [12], considering the Earth rotation, the Coriolis force, and a non-constant gravity model. However, they did not compare the modified IMU preintegration method with the existing methods and illustrated the improvement by considering the Earth rotation [12]. Barrau et al. [19] proposed a preintegration model incorporating the rotating Earth for a high-precision VINS and formulated the preintegration while considering the centrifugal force and Coriolis effect. Their rigorous treatment of the Coriolis effect was achieved using a nontrivial trick, but they did not verify the accuracy improvement by compensating for the Earth rotation in field tests [19]. In their recent work [20], their IMU preintegration was evaluated in a LiDAR-inertial navigation system (LINS) with a high-grade IMU (without giving the specific type), and the results indicate that the Earth rotation is more beneficial for long-term navigation. However, the effect of the Earth rotation on MEMS IMU has not been proven in their works [19], [20]. In [24], the Earth rotation and gravity change were both considered in a preintegration model for VINS. However, the gravity change is usually minor within a city, and thus it can be ignored. As for the Earth rotation compensation, the statistical results indicate that it can be omitted for the MEMS IMU but cannot be neglected for the navigation-grade IMU [24]. According to some dedicated analyses, VINS or LINS involves various parameter settings and multiple impact factors, which may notably disturb the result and confuse the conclusion.

Moreover, the interval of the observations in VINS or LINS is very short (usually within one second), which means the interval of the IMU preintegration is also short. Thus, the constraints from these observations are always applied to the IMU preintegration. Hence, the impacts of the Earth rotation in IMU preintegration cannot be effectively judged, as in [20], [24], especially for the MEMS IMU in [24]. To quantitatively evaluate the accuracy of the IMU preintegration, long-term navigation without other observations should be employed. Hence, the IMU preintegration accuracy can be fully exhibited. The simulated GNSS outage [7] in open-sky areas is an appropriate choice for such evaluation, and it has been widely employed for EKF-based GNSS/INS integration to evaluate the long-term INS accuracy, such as in [28], [29]. Moreover, the simulated GNSS outage has also been used in FGO-Based GNSS/INS/ODO/LiDAR-SLAM to analyze the long-term accuracy of the IMU/ODO preintegration and the LiDAR-SLAM [25].

In this study, we aim to analyze and evaluate the impact of

the Earth rotation compensation on MEMS IMU preintegration. To utilize the method of the simulated GNSS outage, FGO-based GNSS/INS integration, rather than VINS or LINS, is adopted for analysis and evaluation. The EKF-based GNSS/INS integration can constitute a benchmark for the INS accuracy using the method of the simulated GNSS outage, as mentioned above. Hence, the EKF-based GNSS/INS integration is treated as the evaluation baseline. The main contributions of this paper are as follows:

- A sliding-window optimizer for GNSS/INS integration is proposed to fuse GNSS positioning and IMU preintegration under the framework of FGO. The proposed GNSS/INS integration is based on a refined IMU preintegration, in which the Earth rotation has been well compensated.

- The method of the simulated GNSS outage is adopted to quantitatively evaluate the impact of the Earth rotation compensation on IMU preintegration in the proposed GNSS/INS integrations with three field tests in open-sky areas.

- To fully demonstrate the impact of the Earth rotation compensation for different-grade MEMS IMUs, four different MEMS IMUs, including one consumer-grade MEMS chip and three different industrial-grade MEMS modules, are incorporated into the field tests.

- We open-source our FGO-based GNSS/INS integrated navigation system with the refined IMU preintegration, together with our GNSS/INS datasets, which contain four different MEMS IMUs.

The rest of the paper is organized as follows. The next section introduces a refined IMU preintegration model that compensates for the Earth rotation. Section III presents an FGO-based GNSS/INS integrated system based on the refined IMU preintegration. The experiments and results are presented to quantitatively evaluate the impact of the Earth rotation compensation on IMU preintegration in section IV. Finally, the conclusion of this study is presented.

II. REFINED IMU PREINTEGRATION MODEL

Most existing IMU preintegration models ignore the Earth rotation compensation, e.g. in [15], [17], [18], [22], [23], [25]–[27], which is a waste of IMU precision, especially for industrial-grade or high-grade MEMS IMU. Inspired by the precise INS mechanization algorithm [1]–[3], we further refine the IMU preintegration model to compensate for the Earth rotation [24]. This section illustrates the IMU kinematic model first, followed by the IMU motion integration and preintegration processes. Then, the noise propagation of the preintegration measurement is determined, along with the IMU bias-updates procedure.

A. Kinematic Model

An IMU can measure angular rates $\tilde{\omega}_{ib}^b$ and accelerations (specific force) \tilde{f}^b , where b denotes the IMU body frame (b-frame), and i denotes the inertial frame (i-frame). IMU measurements are affected by various errors, including bias, scale factor, non-orthogonality, and white noise [3]. In this study, we only consider additive noise n and slowly varying bias b :

$$\tilde{\omega}_{ib}^b = \omega_{ib}^b + b_g + n_g, \tilde{f}^b = f^b + b_a + n_a, \quad (1)$$

where b_g and b_a represent the gyroscope and accelerometer biases, respectively; n_g and n_a represent the gyroscope and accelerometer white noise, respectively.

Based on the classic high-accuracy INS kinematic model [1]–[3], we omit specific tiny terms and obtain the following reduced model:

$$\begin{aligned} \dot{p}_{wb}^w &= v_{wb}^w, \\ \dot{v}_{wb}^w &= R_b^w f^b + g^w - 2[w_{ie}^w \times] v_{wb}^w, \\ \dot{q}_b^w &= \frac{1}{2} q_b^w \otimes \begin{bmatrix} 0 \\ w_{wb}^b \end{bmatrix}, w_{wb}^b = \omega_{ib}^b - R_w^b \omega_{ie}^w, \end{aligned} \quad (2)$$

where w denotes the world frame (w-frame), which is defined at the initial position of the north-east-down (NED) frame; g^w is the gravity vector in the w-frame; e denotes the Earth frame (e-frame); w_{ie}^w is the Earth rotation rate in the w-frame, and it can be defined as

$$w_{ie}^w = [w_e \cos \varphi_0 \quad 0 \quad -w_e \sin \varphi_0]^T, \quad (3)$$

where w_e is the magnitude of the Earth rotation rate (7.2921158×10^{-5} rad/s) [3]; φ_0 is the geodetic latitude at the initial point. If we omit w_{ie}^w , the kinematic model degenerates to a rough version, as in [23]. The Coriolis acceleration $2[w_{ie}^w \times] v_{wb}^w$ due to the Earth rotation is reserved to improve the integration accuracy. For further reduction of the motion model, readers may refer to [3], [6].

B. Motion Integration

During the integration interval $[t_{k-1}, t_k]$, the duration can be computed by $\Delta t_{k-1,k} = t_k - t_{k-1}$. t_{m-1} and t_m are two consecutive IMU sample times in the interval, as shown in Fig. 1. The incremental angles $\Delta \theta_m$ and incremental velocities $\Delta v_{f,m}^b$ can be computed by integrating the angular rates ω_{ib}^b and accelerations f^b as

$$\Delta \theta_m = \int_{t_{m-1}}^{t_m} \omega_{ib}^b dt, \Delta v_{f,m}^b = \int_{t_{m-1}}^{t_m} f^b dt. \quad (4)$$

It can also be obtained directly from the IMU (some IMUs provide incremental measurements). In this section, the IMU measurements are compensated with the estimated biases, although they are not explicitly expressed in the formulation. Besides, the biases are assumed unchanged throughout the entire preintegration interval.

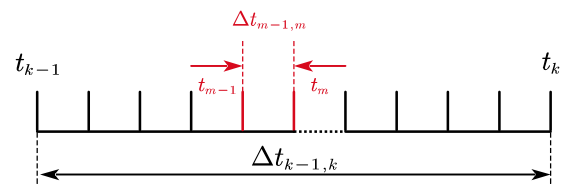


Fig. 1. IMU sample time and preintegration intervals. The preintegration interval is from t_{k-1} to t_k . The interval $\Delta t_{m-1,m} = t_m - t_{m-1}$ is an IMU sample time interval.

The IMU motion integration can be formulated considering the kinematic model in (2) as follows:

$$\begin{aligned} \mathbf{q}_{b_m}^w &= \mathbf{q}_{w_{i(m-1)}}^w(t_m) \otimes \mathbf{q}_{b_{i(m-1)}}^{w_{i(m-1)}} \otimes \mathbf{q}_{b_m}^{b_{i(m-1)}}, \\ \mathbf{v}_{wb_m}^w &= \mathbf{v}_{wb_{m-1}}^w + \int_{t_{m-1}}^{t_m} \mathbf{R}_{w_{i(m-1)}}^w(t) \mathbf{R}_{b_{i(m-1)}}^{w_{i(m-1)}} \mathbf{f}^b dt \\ &\quad + \int_{t_{m-1}}^{t_m} (\mathbf{g}^w - 2\mathbf{w}_{ie}^w \times \mathbf{v}_{wb_t}^w) dt, \\ \mathbf{p}_{wb_m}^w &= \mathbf{p}_{wb_{m-1}}^w + \int_{t_{m-1}}^{t_m} \mathbf{v}_{wb_t}^w dt, \end{aligned} \quad (5)$$

where subscripts m and $m-1$ denote t_m and t_{m-1} , respectively; subscript $w_{i(m-1)}$ denotes the historical w-frame fixed to the i-frame; subscript $b_{i(m-1)}$ denotes the historical b-frame fixed to the i-frame; $\mathbf{q}_{b_{i(m-1)}}^{w_{i(m-1)}} = \mathbf{q}_{b_{m-1}}^w$ denotes the rotation of the b-frame with respect to the w-frame at t_{m-1} . The IMU motion integration (5) can be further written as

$$\begin{aligned} \mathbf{q}_{b_m}^w &= \mathbf{q}_{w_{i(m-1)}}^w(t_m) \otimes \mathbf{q}_{b_{i(m-1)}}^{w_{i(m-1)}} \otimes \mathbf{q}_{b_m}^{b_{i(m-1)}}, \\ \mathbf{v}_{wb_m}^w &= \mathbf{v}_{wb_{m-1}}^w + \frac{1}{2} [\mathbf{R}_{w_{i(m-1)}}^w(t_m) + \mathbf{I}] \mathbf{R}_{b_{i(m-1)}}^{w_{i(m-1)}} \Delta \mathbf{v}_{f,m}^b \\ &\quad + (\mathbf{g}^w - 2\mathbf{w}_{ie}^w \times \mathbf{v}_{wb_{m-1}}^w) \Delta t_{m-1,m}, \\ \mathbf{p}_{wb_m}^w &= \mathbf{p}_{wb_{m-1}}^w + \frac{1}{2} (\mathbf{v}_{wb_{m-1}}^w + \mathbf{v}_{wb_m}^w) \Delta t_{m-1,m}, \end{aligned} \quad (6)$$

where the rotation vector of the b-frame $\mathbf{q}_{b_m}^{b_{i(m-1)}}$ corresponds to the incremental angles $\Delta \theta_m$. The two-sample algorithm can also be incorporated to improve the precision of the motion integration further, see [1]–[3]. The quaternion $\mathbf{q}_{w_{i(m-1)}}^w(t_m)$ or the rotation matrix $\mathbf{R}_{w_{i(m-1)}}^w(t_m)$ is caused by the Earth rotation, and their rotation vector can be expressed as

$$\phi_{w_{i(m-1)}}^w(t_m) = -\mathbf{w}_{ie}^w \Delta t_{m-1,m}. \quad (7)$$

C. IMU Preintegration

For a new IMU measurement, we use (6) to update the motion states (attitude, velocity, and position). However, the IMU motion integration is dependent on the initial motion states, and thus cannot be effectively employed in an FGO framework. The preintegration theory is used to reformulate the model whenever the linearized point (or bias estimation) is changed to avoid repeating the integration multiple times.

To remove the dependence of the initial motion states, the b-frame fixed to the e-frame at the instant t_{k-1} , i.e. $b_{e(k-1)}$, is defined as the reference frame for the refined preintegration model. We can rearrange the motion integration (6) from t_{k-1} to t_k as

$$\begin{aligned} \mathbf{q}_{b_k}^w &= \mathbf{q}_{b_{k-1}}^w \otimes \mathbf{q}_{w_{i(k-1)}}^w(t_k) \otimes \mathbf{q}_{b_{k-1,k}}^{Pre}, \\ \mathbf{v}_{wb_k}^w &= \mathbf{v}_{wb_{k-1}}^w + \mathbf{R}_{b_{e(k-1)}}^w \Delta \mathbf{v}_{k-1,k}^{Pre} + \mathbf{g}^w \Delta t_{k-1,k} - \Delta \mathbf{v}_{g/cor,k-1,k}^w, \\ \mathbf{p}_{wb_k}^w &= \mathbf{p}_{wb_{k-1}}^w + \mathbf{v}_{wb_{k-1}}^w \Delta t_{k-1,k} + \mathbf{R}_{b_{e(k-1)}}^w \Delta \mathbf{p}_{k-1,k}^{Pre} \\ &\quad + 0.5\mathbf{g}^w \Delta t_{k-1,k}^2 - \Delta \mathbf{p}_{g/cor,k-1,k}^w, \end{aligned} \quad (8)$$

where $\mathbf{q}_{w_{i(k-1)}}^w(t_k)$ is the Earth-rotation correction term, which can be obtained from (7); $\Delta \mathbf{v}_{g/cor,k-1,k}^w$ and $\Delta \mathbf{p}_{g/cor,k-1,k}^w$ are the Coriolis correction term for the velocity and position preintegration, respectively. They can be computed as

$$\begin{aligned} \Delta \mathbf{v}_{g/cor,k-1,k}^w &= \int_{t_{k-1}}^{t_k} 2[\mathbf{w}_{ie}^w \times] \mathbf{v}_{wb(t)}^w dt \\ &= 2[\mathbf{w}_{ie}^w \times] (\mathbf{p}_{wb_k}^w - \mathbf{p}_{wb_{k-1}}^w), \\ \Delta \mathbf{p}_{g/cor,k-1,k}^w &= \iint_{t_{k-1}}^{t_k} 2[\mathbf{w}_{ie}^w \times] \mathbf{v}_{wb(t)}^w dt \\ &= 2[\mathbf{w}_{ie}^w \times] \sum_{t_m} [(\mathbf{p}_{wb_m}^w - \mathbf{p}_{wb_{k-1}}^w) \Delta t_{m-1,m}]. \end{aligned} \quad (9)$$

Hence, we can derive the refined preintegration relative to t_{k-1} from (8) as

$$\begin{aligned} \mathbf{q}_{k-1,k}^{Pre} &= \mathbf{q}_{b_k}^{b_{e(k-1)}} = \prod_{t_{k-1}}^{t_k} \mathbf{q}_{b_m}^{b_{e(k-1)}} \\ &= \left(\mathbf{q}_{b_k}^w \right)^{-1} \otimes \mathbf{q}_{w_{i(k-1)}}^w(t_k) \otimes \mathbf{q}_{b_{k-1}}^w, \\ \Delta \mathbf{v}_{k-1,k}^{Pre} &= \int_{t_{k-1}}^{t_k} \mathbf{R}_{b_{e(k-1)}}^{b_{e(k-1)}} \mathbf{f}^b dt \\ &= \sum_{t_m} \frac{1}{2} \left(\mathbf{R}_{b_{k-1}}^w \right)^T \left(\mathbf{R}_{w_{i(m-1)}}^w(t_{m-1}) \right) \mathbf{R}_{b_{k-1}}^w \mathbf{R}_{k-1,m-1}^{Pre} \Delta \mathbf{v}_{f,m}^b \\ &\quad + \left(\mathbf{R}_{b_{k-1}}^w \right)^T (\mathbf{v}_{wb_k}^w - \mathbf{v}_{wb_{k-1}}^w - \mathbf{g}^w \Delta t_{k-1,k} + \Delta \mathbf{v}_{g/cor,k-1,k}^w), \\ \Delta \mathbf{p}_{k-1,k}^{Pre} &= \iint_{t_{k-1}}^{t_k} \mathbf{R}_{b_{e(k-1)}}^{b_{e(k-1)}} \mathbf{f}^b dt \\ &= \sum_{t_m} \frac{1}{2} \left((\Delta \mathbf{v}_{k-1,m-1}^{Pre} + \Delta \mathbf{v}_{k-1,m}^{Pre}) \Delta t_{m-1,m} \right) \\ &\quad + \left(\mathbf{R}_{b_{k-1}}^w \right)^T \left(\mathbf{p}_{wb_k}^w - \mathbf{p}_{wb_{k-1}}^w - \mathbf{v}_{wb_{k-1}}^w \Delta t_{k-1,k} \right. \\ &\quad \left. - 0.5\mathbf{g}^w \Delta t_{k-1,k}^2 + \Delta \mathbf{p}_{g/cor,k-1,k}^w \right), \end{aligned} \quad (10)$$

where $\mathbf{q}_{k-1,k}^{Pre}$, $\Delta \mathbf{v}_{k-1,k}^{Pre}$, and $\Delta \mathbf{p}_{k-1,k}^{Pre}$ are the attitude preintegration, the velocity preintegration, and the position preintegration, respectively. As can be seen in (10), the attitude term $\mathbf{R}_{b_{k-1}}^w$ is used in the refined preintegration because the refined preintegration needs the absolute attitude to incorporate the Earth rotation. The transformation between the reference frame $b_{e(k-1)}$ and the attitude preintegration $\mathbf{q}_{k-1,k}^{Pre}$ can be expressed as follows:

$$\mathbf{q}_{b_k}^{b_{e(k-1)}} = \left(\mathbf{q}_{b_{k-1}}^w \right)^{-1} \otimes \mathbf{q}_{w_{i(k-1)}}^w(t_k) \otimes \mathbf{q}_{b_{k-1}}^w \otimes \mathbf{q}_{k-1,k}^{Pre}, \quad (11)$$

where the w-frame is fixed to the e-frame, and thus we have $\mathbf{q}_{b_{e(k-1)}}^w = \mathbf{q}_{b_{k-1}}^w$.

We obtain the refined preintegration measurements with the Earth rotation compensated from (10). However, the biases are assumed to be unchanged throughout the entire preintegration interval from t_{k-1} to t_k . Therefore, once the bias estimation is changed, we must update the preintegration measurements (section II.E).

D. Noise Propagation

In this part, we derive the statistic of the preintegration error

state vector. The noise covariance strongly influences the MAP estimator because the inverse noise covariance (information matrix) is used to weight the factor in the FGO [18], [23]. We define the error state vector as follows:

$$\delta \mathbf{z}_t = \left[(\delta \mathbf{p}_{k-1,t}^{Pre})^T, (\delta \mathbf{v}_{k-1,t}^{Pre})^T, (\delta \phi_{k-1,t}^{Pre})^T, (\delta \mathbf{b}_{g_t})^T, (\delta \mathbf{b}_{a_t})^T \right]^T, \quad (12)$$

where $\delta \mathbf{p}_{k-1,t}^{Pre}$, $\delta \mathbf{v}_{k-1,t}^{Pre}$, and $\delta \phi_{k-1,t}^{Pre}$ are the position, velocity, and attitude (in terms of the rotation vector) errors of the preintegration measurements, respectively; $\delta \mathbf{b}_{g_t}$ and $\delta \mathbf{b}_{a_t}$ are the gyroscope and accelerometer bias errors, respectively.

With the IMU measurement model expressed in (1), the random noises \mathbf{n}_g and \mathbf{n}_a are modeled as Gaussian white noise processes. The time-varying IMU bias errors are modeled as first-order Gaussian Markov processes [3], according to our experience in classic EKF-based GNSS/INS integration [6]. It should be noted that the biases are assumed unchanged throughout the entire preintegration interval, as mentioned above. Hence, the IMU noise model can be expressed as follows:

$$\begin{aligned} \mathbf{n}_g &\sim \mathcal{N}(\mathbf{0}, \sigma_g^2 \mathbf{I}), \mathbf{n}_a \sim \mathcal{N}(\mathbf{0}, \sigma_a^2 \mathbf{I}), \\ \delta \dot{\mathbf{b}}_{g_t} &= -\frac{1}{\tau_{b_g}} \delta \mathbf{b}_{g_t} + \mathbf{n}_{b_g}, \mathbf{n}_{b_g} \sim \mathcal{N}(\mathbf{0}, \sigma_{b_g}^2 \mathbf{I}), \\ \delta \dot{\mathbf{b}}_{a_t} &= -\frac{1}{\tau_{b_a}} \delta \mathbf{b}_{a_t} + \mathbf{n}_{b_a}, \mathbf{n}_{b_a} \sim \mathcal{N}(\mathbf{0}, \sigma_{b_a}^2 \mathbf{I}), \end{aligned} \quad (13)$$

where τ_b and \mathbf{n}_b are the correlation time and white noise of the first-order Gaussian Markov process, respectively.

Using the error-perturbation method in [3], we can derive the continuous-time dynamics of the preintegration error state as

$$\delta \dot{\mathbf{z}}_t = \mathbf{F}_t \delta \mathbf{z}_t + \mathbf{G}_t \mathbf{w}_t, \quad (14)$$

where \mathbf{w}_t is the noise vector, and it is defined as

$$\mathbf{w}_t = \left[(\mathbf{n}_g)^T, (\mathbf{n}_a)^T, (\mathbf{n}_{b_g})^T, (\mathbf{n}_{b_a})^T \right]^T. \quad (15)$$

By omitting the small second-order terms, the dynamics matrix \mathbf{F}_t is analytically expressed as follows:

$$\mathbf{F}_t = \begin{bmatrix} \mathbf{0} & \mathbf{I} & \mathbf{0} & \mathbf{0} & \mathbf{0} \\ \mathbf{0} & \mathbf{0} & \mathbf{F}_{23} & \mathbf{0} & \mathbf{F}_{25} \\ \mathbf{0} & \mathbf{0} & \mathbf{F}_{33} & -\mathbf{I} & \mathbf{0} \\ \mathbf{0} & \mathbf{0} & \mathbf{0} & -1/\tau_{b_g} \mathbf{I} & \mathbf{0} \\ \mathbf{0} & \mathbf{0} & \mathbf{0} & \mathbf{0} & -1/\tau_{b_a} \mathbf{I} \end{bmatrix}, \quad (16)$$

where the sub-matrix in \mathbf{F}_t is defined as

$$\begin{cases} \mathbf{F}_{23} = -(\mathbf{R}_{b_{k-1}}^w)^T \mathbf{R}_{w_{i(k-1)}}^w (t) \mathbf{R}_{b_{k-1}}^w \hat{\mathbf{R}}_{b_t}^{b_{i(k-1)}} [\hat{\mathbf{f}}^{b(t)} \times], \\ \mathbf{F}_{25} = -(\mathbf{R}_{b_{k-1}}^w)^T \mathbf{R}_{w_{i(k-1)}}^w (t) \mathbf{R}_{b_{k-1}}^w \hat{\mathbf{R}}_{b_t}^{b_{i(k-1)}}, \\ \mathbf{F}_{33} = -[\hat{\mathbf{w}}_{ib(t)}^b \times]. \end{cases} \quad (17)$$

Here, the second-order terms of Δt are also omitted, because Δt is usually a small term. In addition, $\hat{\mathbf{R}}_{b_t}^{b_{i(k-1)}}$ corresponds to the attitude preintegration quaternion in (10), and $\hat{\bullet}$ denotes the estimated term, because we compensate the raw IMU

measurements with the estimated IMU biases as

$$\hat{\mathbf{w}}_{ib(t)}^b = \hat{\mathbf{w}}_{ib(t)}^b - \bar{\mathbf{b}}_{g_{k-1}}, \hat{\mathbf{f}}^{b(t)} = \hat{\mathbf{f}}^{b(t)} - \bar{\mathbf{b}}_{a_{k-1}}. \quad (18)$$

Here, $\bar{\mathbf{b}}_{k-1}$ indicates that the biases used in the preintegration computation are constants, which is why we must incorporate bias updates (section II.E). The noise-input mapping matrix \mathbf{G}_t is expressed as follows:

$$\mathbf{G}_t = \begin{bmatrix} \mathbf{0} & \mathbf{0} & \mathbf{0} & \mathbf{0} \\ \mathbf{0} & \mathbf{G}_{22} & \mathbf{0} & \mathbf{0} \\ -\mathbf{I} & \mathbf{0} & \mathbf{0} & \mathbf{0} \\ \mathbf{0} & \mathbf{0} & \mathbf{I} & \mathbf{0} \\ \mathbf{0} & \mathbf{0} & \mathbf{0} & \mathbf{I} \end{bmatrix}, \quad (19)$$

where the sub-matrix \mathbf{G}_{22} is expressed as

$$\mathbf{G}_{22} = -(\mathbf{R}_{b_{k-1}}^w)^T \mathbf{R}_{w_{i(k-1)}}^w (t) \mathbf{R}_{b_{k-1}}^w \hat{\mathbf{R}}_{b_t}^{b_{i(k-1)}}. \quad (20)$$

Because high-rate IMU data are used, the following numerical approximation can be applied to calculate the transition matrix in the discrete-time form:

$$\Phi_m = \exp(\mathbf{F}(t_{m-1}) \Delta t_{m-1,m}) \approx \mathbf{I} + \mathbf{F}(t_{m-1}) \Delta t_{m-1,m}. \quad (21)$$

In addition, with the continuous-time noise covariance matrix \mathbf{Q}_{t_m} , we can implement a trapezoidal integration to compute the discrete-time noise covariance matrix \mathbf{Q}_m as follows:

$$\mathbf{Q}_{t_m} = \text{diag}(\sigma_g^2 \mathbf{I}, \sigma_a^2 \mathbf{I}, \sigma_{b_g}^2 \mathbf{I}, \sigma_{b_a}^2 \mathbf{I}), \quad (22)$$

$$\mathbf{Q}_m \approx 0.5 (\Phi_m \mathbf{G}_{t_m} \mathbf{Q}_{t_m} \mathbf{G}_{t_m}^T + \mathbf{G}_{t_m} \mathbf{Q}_{t_m} \mathbf{G}_{t_m}^T \Phi_m^T) \Delta t_{m-1,m}, \quad (23)$$

where \mathbf{Q}_{t_m} is the covariance matrix of the noise vector \mathbf{w}_t in (15). Then, the covariance matrix $\Sigma_{k-1,m}^{Pre}$ can be propagated from the initial covariance $\Sigma_{k-1,k-1}^{Pre} = \mathbf{0}$ as follows:

$$\Sigma_{k-1,m}^{Pre} = \Phi_m \Sigma_{k-1,m-1}^{Pre} \Phi_m^T + \mathbf{Q}_m. \quad (24)$$

The first-order Jacobian matrix can also be propagated recursively with the initial Jacobian $\mathbf{J}_{k-1,k-1} = \mathbf{I}$ as

$$\mathbf{J}_{k-1,m} = \Phi_m \mathbf{J}_{k-1,m-1}. \quad (25)$$

Using recursive formulation in (24) and (25), we can obtain the covariance $\Sigma_{k-1,k}^{Pre}$ and the Jacobian $\mathbf{J}_{k-1,k}$, which span the entire preintegration interval.

E. Bias Updates

In sections II.B and II.C, the biases are assumed unchanged throughout the entire preintegration interval. If the bias estimation is changed, we must incorporate bias updates to update the preintegration measurements accordingly. The altered biases can be computed as follows:

$$\delta \mathbf{b}_g = \mathbf{b}_{g_{k-1}} - \bar{\mathbf{b}}_{g_{k-1}}, \delta \mathbf{b}_a = \mathbf{b}_{a_{k-1}} - \bar{\mathbf{b}}_{a_{k-1}}, \quad (26)$$

where $\bar{\mathbf{b}}_{g_{k-1}}$ and $\bar{\mathbf{b}}_{a_{k-1}}$ denote the constant biases in (18), while $\mathbf{b}_{g_{k-1}}$ and $\mathbf{b}_{a_{k-1}}$ denote the newly estimated biases. Hence, we can update the preintegration measurements computed by (10) using first-order expansions

$$\begin{aligned}\hat{\mathbf{q}}_{k-1,k}^{Pre}(\mathbf{b}) &\approx \hat{\mathbf{q}}_{k-1,k}^{Pre}(\bar{\mathbf{b}}) \otimes \begin{bmatrix} 1 \\ \mathbf{J}_{k-1,k}^{\phi, b_g} \delta \mathbf{b}_g \end{bmatrix}, \\ \Delta \hat{\mathbf{v}}_{k-1,k}^{Pre}(\mathbf{b}) &\approx \Delta \hat{\mathbf{v}}_{k-1,k}^{Pre}(\bar{\mathbf{b}}) + \mathbf{J}_{k-1,k}^{v, b_g} \delta \mathbf{b}_g + \mathbf{J}_{k-1,k}^{v, b_a} \delta \mathbf{b}_a, \\ \Delta \hat{\mathbf{p}}_{k-1,k}^{Pre}(\mathbf{b}) &\approx \Delta \hat{\mathbf{p}}_{k-1,k}^{Pre}(\bar{\mathbf{b}}) + \mathbf{J}_{k-1,k}^{p, b_g} \delta \mathbf{b}_g + \mathbf{J}_{k-1,k}^{p, b_a} \delta \mathbf{b}_a,\end{aligned}\quad (27)$$

where the left-hand sides of (27) are the preintegration measurements updated using the newly estimated biases; the first term of each formulation on the right side of (27) is the preintegration measurements computed using the constant biases; $\mathbf{J}_{k-1,k}^{p, b_g}$ is the sub-matrix of $\mathbf{J}_{k-1,k}$, the location of which corresponds to $\delta \mathbf{p}_{k-1,k}^{Pre} / \delta \mathbf{b}_{g_{k-1}}$ (the same definition applies to $\mathbf{J}_{k-1,k}^{p, b_a}$, $\mathbf{J}_{k-1,k}^{v, b_g}$, $\mathbf{J}_{k-1,k}^{v, b_a}$, and $\mathbf{J}_{k-1,k}^{\phi, b_g}$).

Finally, we obtain an accurate IMU preintegration model derived from the classic INS kinematic model while considering the Earth rotation compensation. In addition, the noise propagation of the preintegration measurement is described in detail. The bias-updates process is also discussed.

III. FGO-BASED GNSS/INS INTEGRATION

In this section, we construct an FGO-based GNSS/INS integrated navigation system using the refined IMU preintegration model described in the previous section to quantitatively evaluate the impact of the Earth rotation compensation on IMU preintegration.

A. Formulation

An FGO-based sliding-window optimizer is utilized to process the IMU preintegration and GNSS positioning measurements, as depicted in the abstract. The IMU states in the sliding window are defined as $\mathbf{X} = [\mathbf{x}_0, \mathbf{x}_1, \dots, \mathbf{x}_n]$, where \mathbf{x}_k is expressed as

$$\mathbf{x}_k = \left[\left(\mathbf{p}_{wb_k}^w \right)^T, \left(\mathbf{v}_{wb_k}^w \right)^T, \left(\mathbf{q}_{b_k}^w \right)^T, \left(\mathbf{b}_{g_k} \right)^T, \left(\mathbf{b}_{a_k} \right)^T \right]^T. \quad (28)$$

Here, the state \mathbf{x}_k includes the position, velocity, and attitude of the IMU in the w-frame, along with the gyroscope and accelerometer biases, where $k \in [0, n]$. The n is the size of the sliding window. We add an IMU preintegration factor into the sliding window at each GNSS second, though the GNSS positioning factor may be absent due to outages. In other words, the interval of each preintegration factor is one second. Besides, as depicted in the abstract, the IMU preintegration factors are connected one by one, which means it is time-continuous. It is conducive for IMU biases estimation because the IMU biases are also incorporated into the IMU preintegration factors, see section III.B.

We minimize the sum of the prior and the Mahalanobis norm of all measurement residuals to obtain the following MAP estimation:

$$\min_{\mathbf{X}} \left\{ \left\| \mathbf{r}_p - \mathbf{H}_p \mathbf{X} \right\|^2 + \sum_{k \in [1, n]} \left\| \mathbf{r}_{Pre} \left(\hat{\mathbf{z}}_{k-1, k}^{Pre}, \mathbf{X} \right) \right\|_{\Sigma_{k-1, k}^{Pre}}^2 + \sum_{i \in [0, m]} \left\| \mathbf{r}_{GNSS} \left(\hat{\mathbf{z}}_i^{GNSS}, \mathbf{X} \right) \right\|_{\Sigma_i^{GNSS}}^2 \right\}, \quad (29)$$

where \mathbf{r}_{Pre} and \mathbf{r}_{GNSS} are the residuals for the IMU preintegration factors and GNSS positioning factors, respectively; $m+1 (m \leq n)$ is the number of GNSS positioning factors; $\{\mathbf{r}_p, \mathbf{H}_p\}$ represents the prior information from the marginalization (section III.D). Ceres solver [30] is used for solving this nonlinear-optimization problem.

B. IMU Preintegration Factor

With the preintegration measurements in (10) and the bias-updated preintegration measurements in (27), we can compute the residual of the IMU preintegration factor as

$$\begin{aligned}\mathbf{r}_{Pre} \left(\hat{\mathbf{z}}_{k-1, k}^{Pre}, \mathbf{X} \right) &= \begin{bmatrix} \left(\mathbf{R}_{b_{k-1}}^w \right)^T \left(\mathbf{p}_{wb_k}^w - \mathbf{p}_{wb_{k-1}}^w - \mathbf{v}_{wb_{k-1}}^w \Delta t_{k-1, k} - \Delta \hat{\mathbf{p}}_{k-1, k}^{Pre} \right) \\ \left(\mathbf{R}_{b_{k-1}}^w \right)^T \left(\mathbf{v}_{wb_k}^w - \mathbf{v}_{wb_{k-1}}^w - \mathbf{g}^w \Delta t_{k-1, k} + \Delta \mathbf{v}_{g/cor, k-1, k}^w \right) \\ 2 \left[\left(\mathbf{q}_{b_k}^w \right)^{-1} \otimes \mathbf{q}_{wb_{k-1}}^w \left(t_k \right) \otimes \mathbf{q}_{b_{k-1}}^w \otimes \hat{\mathbf{q}}_{k-1, k}^{Pre} \right]_v \\ \mathbf{b}_{g_k} - \mathbf{b}_{g_{k-1}} \\ \mathbf{b}_{a_k} - \mathbf{b}_{a_{k-1}} \end{bmatrix},\end{aligned}\quad (30)$$

where $2[\cdot]_v$ is the algorithm to extract the (small-angle) rotation vector of a quaternion; $\Delta \mathbf{v}_{g/cor, k-1, k}^w$ and $\Delta \mathbf{p}_{g/cor, k-1, k}^w$ are the Coriolis correction term for the velocity and position preintegration, respectively, as defined in (9). The gyroscope and accelerometer biases are also included in the residual terms for online estimation and correction. The wheeled odometer can also be integrated into the IMU preintegration [25], which is included in our source codes. The covariance $\Sigma_{k-1, k}^{Pre}$ of the IMU preintegration factor is derived from section II.D.

C. GNSS Positioning Factor

The positioning result in geodetic coordinates $\hat{\mathbf{p}}_{GNSS, i}^e$ and its covariance Σ_i^{GNSS} can be obtained from the GNSS receiver. The geodetic coordinates can be converted to the local w-frame as $\hat{\mathbf{p}}_{GNSS, i}^w$ [3]. Hence, the residual of the GNSS positioning factor can be expressed as follows:

$$\mathbf{r}_{GNSS} \left(\hat{\mathbf{z}}_i^{GNSS}, \mathbf{X} \right) = \mathbf{p}_{wb_i}^w + \mathbf{R}_{b_i}^w \mathbf{l}_{GNSS}^b - \hat{\mathbf{p}}_{GNSS, i}^w, \quad (31)$$

where \mathbf{l}_{GNSS}^b is the GNSS antenna lever-arm expressed in the b-frame, and the covariance Σ_i^{GNSS} corresponds to the NED direction of the w-frame.

D. Marginalization

We incorporate marginalization to bound the computational complexity of the sliding-window optimizer. If the number of the IMU preintegration factors exceeds the threshold (the sliding-window size), we marginalize the oldest IMU state. Besides, the IMU preintegration and GNSS positioning measurements corresponding to the marginalized state are converted into a prior factor. For more details on the marginalization in sliding-window optimization, readers may

refer to [31].

This section incorporates the refined IMU preintegration model into an FGO-based GNSS/INS integrated navigation system. The residuals of the IMU preintegration factor and GNSS positioning factor are all computed as analytical expressions. The marginalization approach is also adopted to reduce the computational cost.

IV. EXPERIMENTS AND RESULTS

The impact of the Earth rotation on MEMS-IMU preintegration is evaluated in this section, using the simulated GNSS outage [7]. The EKF-based GNSS/INS integration can constitute a benchmark of the potential INS accuracy because the Earth rotation compensation, Coriolis acceleration, and various precise correction are fully considered in the precise INS mechanization [1]–[3], as mentioned above. Consequently, the classic EKF-based GNSS/INS integrated navigation system using the precise INS mechanization was adopted as an evaluation baseline.

A. Vehicle Experiment Setup

Three vehicle tests were conducted in an open-sky area, with durations of 2325, 1617, and 2333 seconds, respectively. The trajectories of the tests are depicted in Fig. 2. The average vehicle speed throughout the travel period was approximately 10 m/s, as shown in Fig. 3. Allowing at least 500 seconds for navigation-system initialization, we intentionally blocked the GNSS positioning for 60 seconds every 150-seconds in the post-processing procedure. Each test sequence was processed twice with different first-outage start times. We finally obtained 61 outages in total, and the statistical results for the maximum position-drift error during each simulated GNSS outage were adopted to evaluate the system accuracy. Note that the attitude drift was not considered here because the position drift is a sensitive and comprehensive indicator of the inherent accuracy

of the entire navigation system, while the attitude drift is not [7]. Such evaluation method is widely used for GNSS/INS integration, such as in [25], [28], [29]. Specifically, the root-mean-square errors (RMSEs) of the maximum horizontal- and vertical-drift errors in each GNSS outage were used.

Four different MEMS IMUs were employed in the tests: ICM20602, a consumer-grade MEMS chip; ADIS16460, ADIS16465, and HGuide-i300, which are all industrial-grade MEMS modules with precision differences. The four IMUs were attached to the exact vehicle and sampled at the same sample rate of 200 Hz. The GNSS positioning results used in the tests were Post-Processed Kinematic (PPK) [3] solutions to get the best GNSS results with centimeter-level accuracy. The ground truth was obtained from a navigation-grade GNSS/INS integrated navigation system.

The main parameters of the four MEMS IMUs are listed in Table I. The bias instability parameters for ICM20602 were derived from the tested Allan-variance curves; the parameters for ADIS16460, ADIS16465, and HGuide-i300, were obtained from the corresponding data sheets. Note that the magnitudes of the gyroscope-bias instabilities in Table I are all less than the Earth rotation rate of 15 °/h, which indicates the necessity of considering the Earth rotation in IMU preintegration; otherwise, the gyroscope precision will be somewhat wasted. As for the acceleration-bias instabilities, they are all less than 0.001g, where g is the normal gravity. As can be seen, the bias-instability parameters for these MEMS IMUs are all very ideal, mainly because they are obtained from the Allan-variance curves using the static data. These parameters cannot reflect the IMU precision exactly, according to the results in section IV.B. For example, the HGuide-i300 is the best IMU, but its bias-instability parameters are even larger than that of the ADIS16465.

Parameter tuning was conducted to mitigate the impacts of



Fig. 2. Trajectories of the vehicle tests.

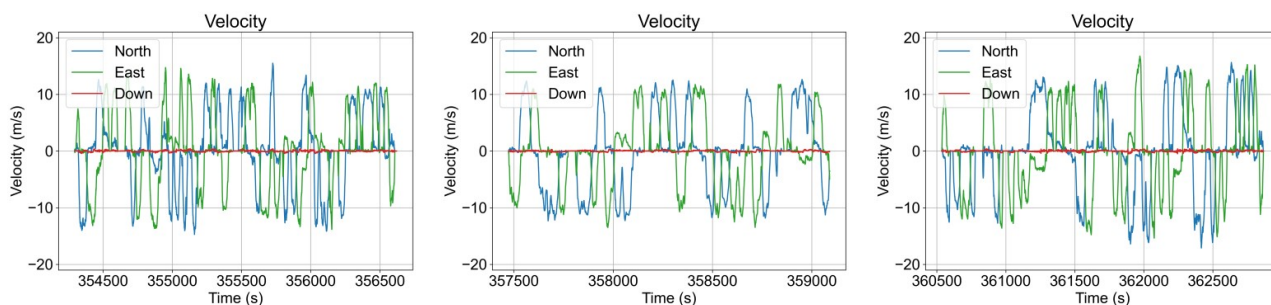


Fig. 3. Velocity profiles of the vehicle tests.

TABLE I

BIAS INSTABILITY PARAMETERS OF MEMS IMUS

IMU	ICM20602 (InvenSense)	ADIS16460 (ADI)	ADIS16465 (ADI)	HGuide-i300 (Honeywell)
Gyroscope (°/h 1σ)	10.0	8.0	2.0	3.0
Acceleration (mGal 1σ)	30.0	200.0	3.6	20

The bias instability parameter for ICM20602 was obtained from the tested Allan variance curve; the parameters for ADIS16460, ADIS16465, and HGuide-i300, were obtained from the corresponding device data-sheets. Here, 1 mGal is equal to 1.0×10^{-5} m/s².

TABLE II

PROCESSING MODE CONFIGURATIONS

Mode	Type	Description
M0 (EKF-Base)	EKF	A classic EKF-based GNSS/INS integrated navigation algorithm using the high-precision INS mechanization compensating for the Earth rotation.
M1 (EKF-Rough)	EKF	An EKF-based GNSS/INS integrated navigation algorithm using a rough INS mechanization without compensating for the Earth rotation.
M2 (FGO-Refined)	FGO	A mode incorporating the refined preintegration that compensates the Earth rotation, as introduced in Section II.
M3 (FGO-Rough)	FGO	A mode incorporating a rough preintegration without compensating the Earth rotation.

the IMU noise parameters, including σ_g , σ_a , σ_{b_g} , and σ_{b_a} , as defined in (13). Note that these parameters are equally applied in (13) for M0, M1, M2, and M3. The correlation-times τ_{b_g} and τ_{b_a} were set to 1 hour for all the four MEMS IMUs without tuning, according to our previous experience. Batch processes based on grid searching were implemented to obtain the optimal parameters for these parameters in each mode by minimizing the RMSEs of the position-drift errors during the simulated GNSS outages. The optimized parameters of the four MEMS IMUs can be found on our GitHub page. The turn-on biases of these IMUs are not modeled in the proposed FGO-based integration or the EKF-based integration. The first 500 seconds of each test are employed for the system initialization to mitigate the effects of the turn-on biases in the experiments. More specifically, the simulated GNSS outages are conducted after the system has converged.

Four processing modes were adopted for the tests: EKF-based integration with the high-precision INS mechanization (baseline), EKF-based integration with the rough INS mechanization, FGO-based integration with the refined IMU preintegration, and FGO-based integration with the rough IMU preintegration, labeled with M0, M1, M2, and M3, respectively, as shown in Table II. The FGO-based modes for M2 and M3 are described in section III. The M0 was treated as the baseline because its accuracy has been well proven to constitute a benchmark for the potential INS accuracy [3], as noted above. M1 was adopted to evaluate the effect of the Earth rotation compensation on INS mechanization, acting as a comparison of M3.

We conducted dedicated experiments to evaluate the influence of the sliding-window size n . The results indicate that the sliding-window size has little impact on the accuracy of the FGO-based GNSS/INS integration systems in this

TABLE III

RMSEs OF THE HORIZONTAL AND VERTICAL DRIFTS IN 60S GNSS OUTAGES CONCERNING THE SLIDING-WINDOW SIZE IN THE M2 (METERS)

Size (Seconds)	5		10		20		50	
	Hor.	Ver.	Hor.	Ver.	Hor.	Ver.	Hor.	Ver.
ICM20602	45.30	12.89	45.29	12.89	45.30	12.89	45.31	12.89
ADIS16460	20.15	2.26	20.15	2.26	20.15	2.26	20.15	2.26
ADIS16465	9.14	0.96	9.14	0.96	9.14	0.96	9.14	0.96
HGuide-i300	7.70	2.14	7.71	2.14	7.71	1.14	7.71	2.14

The ‘‘Hor.’’ and ‘‘Ver.’’ denote the horizontal and vertical drifts, respectively.

TABLE IV

RMSEs OF THE HORIZONTAL AND VERTICAL DRIFTS IN 60S GNSS OUTAGES (METERS)

IMU	M0 (EKF-Base)		M1 (EKF-Rough)		M2 (FGO-Refined)		M3 (FGO-Rough)	
	Hor.	Ver.	Hor.	Ver.	Hor.	Ver.	Hor.	Ver.
ICM20602	45.10	12.89	50.95	13.09	45.30	12.89	51.03	13.09
ADIS16460	20.03	2.30	29.03	2.47	20.15	2.26	29.19	2.43
ADIS16465	9.13	0.97	22.29	1.50	9.14	0.96	22.43	1.50
HGuide-i300	7.68	2.15	23.01	2.99	7.71	2.14	23.09	2.98

The ‘‘Hor.’’ and ‘‘Ver.’’ denote the horizontal and vertical drifts, respectively.

experiment, as exhibited in Table III. However, it might affect the system accuracy in GNSS-challenging environments, such as in [13]. Hence, the sliding-window size should be appropriate for the possible applications in GNSS-challenging environments. Therefore, the sliding-window sizes for M2 and M3 were set to 20 seconds to bound the computation complexity. The interval of each preintegration factor is one second, and the sample rates for the four MEMS IMUs are 200 Hz, as mentioned above.

B. Results and Discussions

After the parameter tuning, we obtained the RMSEs of the position-drift errors for the four MEMS IMUs. As shown in Table IV, the RMSEs for M0 and M2 are almost identical for all the four IMUs; however, the RMSEs for M1 and M3 are much worse than those of the other two modes, especially for the horizontal drifts. These results demonstrate that the refined preintegration model can achieve the same accuracy as the classic high-accuracy INS algorithm once the Earth rotation has been compensated. In contrast, the IMU preintegration accuracy may degrade significantly without the Earth rotation compensation. According to the horizontal-drift RMSEs in M0, HGuide-i300 and ICM20602 are the best- and worst-performing of the four IMUs in this experiment. As expected in section II, the higher grade IMU has the gyroscope bias error much smaller than the Earth rotation rate; therefore, it should care more about the Earth rotation compensation than the lower grade IMU. In other words, higher grade IMUs need the refined IMU preintegration more. On the contrary, lower grade IMU has gyroscope bias error similar to or even larger than the Earth rotation rate. Hence, their dominant error comes from the sensor instead of the Earth rotation compensation in the algorithm. In other words, lower grade IMU should not be

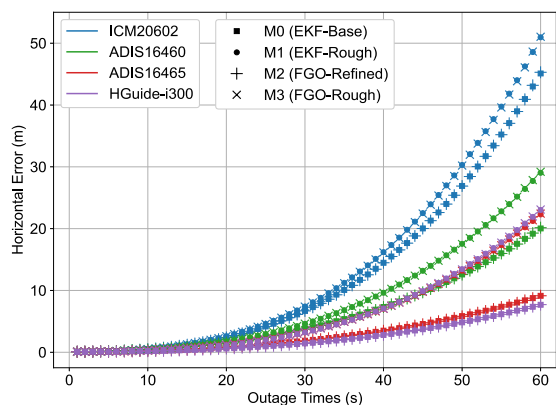


Fig. 4. The horizontal-drift error with respect to outage times for different IMUs in different processing modes. Different colors denote different IMUs. Different markers represent different processing modes.

very sensitive to the IMU preintegration improvement. The results in Table IV well confirm these conclusions. Specifically, the accuracy degradation in M3 is more significant for the better-performing IMU (e.g. HGuide-i300) than the worse-performing IMU (e.g. ICM20602). The same conclusion can be obtained for the EKF-based integration by comparing the results in M0 and M1. It indicates that the Earth rotation compensation is also a dominant factor for the INS mechanization in the EKF-based integration. Moreover, the RMSEs in M1 and M3 are nearly identical for all the MEMS IMUs, demonstrating that the Earth rotation compensation almost plays the same role in FGO-based integration and EKF-based integration.

The above results can be further proven in Fig. 4, illustrating the horizontal-drift error concerning the outage times for the four IMUs in different processing modes. The horizontal-drift error concerning different outage times in M0 and M2 are almost the same for all these four MEMS IMUs. In contrast, the horizontal-drift error in M1 and M3 is far more significant, as depicted in Fig. 4. Besides, M1 and M3 also exhibit the same accuracy concerning different outage times. Moreover, the better the IMU is, the more notable accuracy degradation in M0 and M3 is. The results demonstrate that the Earth rotation compensation is a significant factor that impacts the accuracy of the IMU preintegration and the INS mechanization. Specifically, the accuracy of the IMU preintegration and the INS mechanization can be entirely performed by compensating for the Earth rotation; otherwise, notable accuracy degradation will occur, especially for industrial-grade or high-grade MEMS IMUs. Moreover, it can be inferred that the impact of the Earth rotation compensation can be more significant when the GNSS-outage time is longer.

We also calculated the horizontal-drift differences between M2 and M3 to quantitatively evaluate the impact of the Earth rotation compensation on IMU preintegration. As shown in Table IV, the better the IMU performance is, the more significant the horizontal-drift difference; this result corresponds to the previous conclusion. Without compensating for the Earth rotation, the IMU accuracy is sometimes wasted. Therefore, the horizontal-drift error increases significantly for FGO-based integration, as indicated by the rough preintegration result (M3). More specifically, the

TABLE V
HORIZONTAL-DRIFT DIFFERENCES BETWEEN M2 (FGO-REFINED) AND M3 (FGO-ROUGH) IN 60S GNSS OUTAGES

IMU	Difference (m)	Percentage (%)
ICM20602	5.73	12.65%
ADIS16460	9.04	44.86%
ADIS16465	13.29	145.40%
HGuide-i300	15.38	199.48%

The difference is defined as $M3-M2$, and the percentage is defined as $(M3-M2)/M2*100\%$.

horizontal-drift error increases by 10~200% for different-grade MEMS IMUs, when the GNSS-outage time is 60 seconds. Such differences can be more notable if the GNSS-outage time is longer, as can be seen in Fig. 4. Consequently, we can conclude that the Earth rotation is a major factor impacting the IMU-preintegration accuracy in the graph factor optimization and should not be neglected.

V. CONCLUSION

In this study, we propose an FGO-based GNSS/INS integrated navigation system in which GNSS positioning and IMU preintegration are tightly fused in a sliding-window optimizer. The Earth rotation compensation has been well considered in the employed IMU preintegration model. Using the simulated GNSS outage, the impact of the Earth rotation compensation on MEMS-IMU preintegration was analyzed and evaluated. The results indicate that the Earth rotation compensation may notably affect the IMU preintegration and the INS mechanization accuracy. The IMU preintegration accuracy can be significantly improved to the precise INS mechanization level by compensating for the Earth rotation. In contrast, the existing rough IMU preintegration without the Earth rotation compensation yields notable accuracy degradation. In addition, the accuracy degradation can be more severe if the GNSS-outage time is longer. Consequently, the Earth rotation compensation is the primary factor to be considered in IMU preintegration to maintain the IMU precision, especially for industrial-grade MEMS IMU or high-grade IMU. The conclusion can also be transferred to other integrated navigation systems incorporating IMU preintegration, such as VINS and LINS.

REFERENCES

- [1] P. G. Savage, "Strapdown Inertial Navigation Integration Algorithm Design Part 1: Attitude Algorithms," *J. Guid. Control Dyn.*, vol. 21, no. 1, pp. 19–28, 1998.
- [2] P. G. Savage, "Strapdown Inertial Navigation Integration Algorithm Design Part 2: Velocity and Position Algorithms," *J. Guid. Control Dyn.*, vol. 21, no. 2, pp. 208–221, 1998.
- [3] P. D. Groves, *Principles of GNSS, inertial, and multisensor integrated navigation systems*. Boston: Artech House, 2008.
- [4] C. Shen *et al.*, "Seamless GPS/Inertial Navigation System Based on Self-Learning Square-Root Cubature Kalman Filter," *IEEE Trans. Ind. Electron.*, vol. 68, no. 1, pp. 499–508, 2021.
- [5] B. Gao, G. Hu, Y. Zhong, and X. Zhu, "Cubature Kalman Filter With Both Adaptability and Robustness for Tightly-Coupled GNSS/INS Integration," *IEEE Sens. J.*, vol. 21, no. 13, pp. 14997–15011, Jul. 2021.

[6] Q. Zhang, X. Niu, H. Zhang, and C. Shi, "Algorithm Improvement of the Low-End GNSS/INS Systems for Land Vehicles Navigation," *Math. Probl. Eng.*, vol. 2013, pp. 1–12, 2013.

[7] X. Niu, H. Zhang, C. Shi, K.-W. Chiang, and N. El-Sheimy, "A proposed evaluation standard for the navigation results of MEMS INS/GPS integrated systems," in *Proceedings of the International Symposium on GPS/GNSS*, 2010, pp. 1–5.

[8] C. Cadena *et al.*, "Past, Present, and Future of Simultaneous Localization and Mapping: Toward the Robust-Perception Age," *IEEE Trans. Robot.*, vol. 32, no. 6, pp. 1309–1332, Dec. 2016.

[9] G. Huang, "Visual-Inertial Navigation: A Concise Review," in *2019 International Conference on Robotics and Automation (ICRA)*, May 2019, pp. 9572–9582.

[10] D. Rouzard and J. Skaloud, "Rigorous Integration of Inertial Navigation with Optical Sensors by Dynamic Networks," *Navigation*, vol. 58, no. 2, pp. 141–152, Jun. 2011.

[11] D. A. Cucci, M. Rehak, and J. Skaloud, "Bundle adjustment with raw inertial observations in UAV applications," *ISPRS J. Photogramm. Remote Sens.*, vol. 130, pp. 1–12, Aug. 2017.

[12] D. A. Cucci and J. Skaloud, "ON RAW INERTIAL MEASUREMENTS IN DYNAMIC NETWORKS," *ISPRS Ann. Photogramm. Remote Sens. Spat. Inf. Sci.*, vol. IV-2/W5, pp. 549–557, May 2019.

[13] W. Wen, T. Pfeifer, X. Bai, and L.-T. Hsu, "Factor graph optimization for GNSS/INS integration: A comparison with the extended Kalman filter," *NAVIGATION*, vol. 68, no. 2, pp. 315–331, 2021.

[14] S. Zhao, Y. Chen, and J. A. Farrell, "High-Precision Vehicle Navigation in Urban Environments Using an MEM's IMU and Single-Frequency GPS Receiver," *IEEE Trans. Intell. Transp. Syst.*, vol. 17, no. 10, pp. 2854–2867, Oct. 2016.

[15] K. Eckenhoff, P. Geneva, and G. Huang, "Closed-form preintegration methods for graph-based visual-inertial navigation," *Int. J. Robot. Res.*, vol. 38, no. 5, pp. 563–586, Apr. 2019.

[16] W. Wen, X. Bai, Y. C. Kan, and L.-T. Hsu, "Tightly Coupled GNSS/INS Integration via Factor Graph and Aided by Fish-Eye Camera," *IEEE Trans. Veh. Technol.*, vol. 68, no. 11, pp. 10651–10662, Nov. 2019.

[17] T. Lupton and S. Sukkarieh, "Visual-Inertial-Aided Navigation for High-Dynamic Motion in Built Environments Without Initial Conditions," *IEEE Trans. Robot.*, vol. 28, no. 1, pp. 61–76, Feb. 2012.

[18] C. Forster, L. Carlone, F. Dellaert, and D. Scaramuzza, "On-Manifold Preintegration for Real-Time Visual-Inertial Odometry," *IEEE Trans. Robot.*, vol. 33, no. 1, pp. 1–21, Feb. 2017.

[19] A. Barrau and S. Bonnabel, "A Mathematical Framework for IMU Error Propagation with Applications to Preintegration," in *2020 IEEE International Conference on Robotics and Automation (ICRA)*, May 2020, pp. 5732–5738.

[20] M. Brossard, A. Barrau, P. Chauchat, and S. Bonnabel, "Associating Uncertainty to Extended Poses for on Lie Group IMU Preintegration With Rotating Earth," *IEEE Trans. Robot.*, pp. 1–18, 2021.

[21] Y. Luo, C. Guo, and J. Liu, "Equivariant filtering framework for inertial-integrated navigation," *Satell. Navig.*, vol. 2, no. 1, p. 30, Dec. 2021.

[22] S. Shen, N. Michael, and V. Kumar, "Tightly-coupled monocular visual-inertial fusion for autonomous flight of rotorcraft MAVs," in *2015 IEEE International Conference on Robotics and Automation (ICRA)*, May 2015, pp. 5303–5310.

[23] T. Qin, P. Li, and S. Shen, "VINS-Mono: A Robust and Versatile Monocular Visual-Inertial State Estimator," *IEEE Trans. Robot.*, vol. 34, no. 4, pp. 1004–1020, Aug. 2018.

[24] J. Jiang, X. Niu, and J. Liu, "Improved IMU Preintegration with Gravity Change and Earth Rotation for Optimization-Based GNSS/VINS," *Remote Sens.*, vol. 12, no. 18, Art. no. 18, Jan. 2020.

[25] L. Chang, X. Niu, and T. Liu, "GNSS/IMU/ODO/LiDAR-SLAM Integrated Navigation System Using IMU/ODO Pre-Integration," *Sensors*, vol. 20, no. 17, p. 4702, Aug. 2020.

[26] S. Bai, J. Lai, P. Lyu, Y. Cen, and B. Ji, "Improved Preintegration Method for GNSS/IMU/In-Vehicle Sensors Navigation using Graph Optimization," *IEEE Trans. Veh. Technol.*, pp. 1–1, 2021.

[27] J. Henawy, Z. Li, W.-Y. Yau, and G. Seet, "Accurate IMU Factor Using Switched Linear Systems for VIO," *IEEE Trans. Ind. Electron.*, vol. 68, no. 8, pp. 7199–7208, Aug. 2021.

[28] L. Wang, H. Tang, T. Zhang, Q. Chen, J. Shi, and X. Niu, "Improving the Navigation Performance of the MEMS IMU Array by Precise Calibration," *IEEE Sens. J.*, vol. 21, no. 22, pp. 26050–26058, 2021.

[29] H. Tang, X. Niu, T. Zhang, Y. Li, and J. Liu, "OdoNet: Untethered Speed Aiding for Vehicle Navigation Without Hardware Wheeled Odometer," *IEEE Sens. J.*, vol. 22, no. 12, pp. 12197–12208, Jun. 2022.

[30] Agarwal, Sameer, Mierle, and Keir, "Ceres Solver — A Large Scale Non-linear Optimization Library." [Online]. Available: <http://ceres-solver.org/>

[31] J. Engel, V. Koltun, and D. Cremers, "Direct Sparse Odometry," *IEEE Trans. Pattern Anal. Mach. Intell.*, vol. 40, no. 3, pp. 611–625, Mar. 2018.



Hailiang Tang received the B.E. and M.E. degrees from Wuhan University, China, in 2017 and 2020, respectively. He is currently pursuing a Ph.D. degree in communication and information systems with the GNSS Research Center, Wuhan University. His current research interests include GNSS/INS integration, deep learning, visual SLAM, and autonomous robotics system.



Tisheng Zhang is an associate professor in GNSS Research Center at Wuhan University, China. He holds a B.Sc. and a Ph.D. in Communication and Information System from Wuhan University, Wuhan, China, in 2008 and 2013, respectively. From 2018 to 2019, he was a Post Doctor at the Hong Kong Polytechnic University. His research interests focus on the fields of GNSS receiver and multi-sensor deep integration.



Xiaoji Niu received his bachelor's and Ph.D. degrees from the Department of Precision Instruments, Tsinghua University, in 1997 and 2002, respectively. He is currently a Professor with the GNSS Research Center, Wuhan University, China. He did post-doctoral research with the University of Calgary and worked as a Senior Scientist in SiRF Technology Inc. He has published more than 90 academic papers and owns 28 patents. He leads a multi-sensor navigation group focusing on GNSS/INS integration, low-cost navigation sensor fusion, and its new applications.



Fan Jing received the B.Eng. degree from Jilin University in 2018 and the M.Eng. degree from Wuhan University in 2021, respectively. She is pursuing her Ph.D. degree in geodesy and survey engineering with the GNSS Research Center. Her current research interests focus on GNSS positioning technology, tightly coupled GNSS/INS integration technology, and visual SLAM.



Jingnan Liu, member of the Chinese Academy of Engineering, professor, Ph. D supervisor. He is an expert in geodesy and surveying engineering with a specialty in GNSS technology and applications. He has been engaged in researching geodetic theories and applications, including national coordinate system establishment, GNSS technology and software development, and large project implementation. Over the past few decades, he has been engaged in researching geodetic theories and applications. He has published more than 150 academic papers and supervised over 100 postgraduates.